Available online at www.sciencedirect.com
ScienceDirect
Trans. Nonferrous Met. Soc. China 34(2024) 94−107
Transactions of Nonferrous Metals Society of China
www.tnmsc.cn

Effect of heat treatment on microstructure and mechanical property of roll-bonded 1060/7N01/1060 laminates

Shun-qiang LI[1#], Guo-sheng SUN[1#], Rui-sheng ZHANG[1], Xiao CHENG[1], Ji-zi LIU[1,2]

1. Nano and Heterogeneous Materials Center, School of Materials Science and Engineering, Nanjing University of Science and Technology, Nanjing 210094, China;
2. Center of Analytical Facilities, Nanjing University of Science and Technology, Nanjing 210094, China

Received 4 July 2022; accepted 15 December 2022

Abstract: 1060/7N01/1060 laminated composites with reliable bonding interfaces were successfully fabricated via single-pass hot rolling at 475 °C. The effects of layer thickness ratios on microstructure and mechanical property of synthesized laminates were studied using scanning electron microscope, transmission electron microscope and electron backscattered diffraction technique accompanied with hardness and tensile testing. Moreover, microstructure and mechanical property of DCR (direct cold rolling) and ACR (solution annealing and peak ageing plus cold rolling) samples were also explored. The results show that layer thickness ratios have little effect on microstructure of each layer in hot-rolled sheets, and their mechanical properties are consistent with theoretical predictions based on the rule of mixture. In comparison, extra heat treatment has no obvious effect on grain size of pure aluminium layers. However, smaller strip-like grains along with dispersed, finer precipitates are formed in 7N01 layer of ACR samples, leading to stronger grain refinement strengthening, precipitation strengthening and dislocation strengthening.

Key words: 7N01 aluminium alloy; pure aluminium; laminated composite; bonding interface; ageing; mechanical properties

1 Introduction

As one kind of the structural materials, Al-alloys, with high specific strength, have been widely used in many fields including civil aviation, railway traffic and lightweight automobile and so on [1,2]. As a main strengthening approach, alloying can effectively improve the strength of Al-alloys. However, the contribution of further adding new alloying elements or increasing their contents to the strength improvement of mature Al-alloy systems has been very limited. Additionally, this may lead to the increase of stress corrosion sensitivity, and decrease of fracture toughness and fatigue life [3−5]. Since the concept of plainified materials has been proposed to meet the demand for resource sustainability [6], it must be very meaningful to explore approaches to combine advantages of different materials (such as the superior corrosion resistance and good plastic processing performance of pure Al, and the good strength−ductility combination of Al-alloys) by simple manufacturing processes. The development of metallic laminated composites is one of the representative achievements.

Many ways, including explosive welding [7−9], extrusion [10,11], diffusion bonding [12,13], friction stir welding [14], electrodeposition [15], physical vapor deposition [16] and magnetic sputtering [17], have been developed depending on material type to fabricate laminated composites

[#]Shun-qiang LI and Guo-sheng SUN contributed equally to this work
Corresponding author: Ji-zi LIU, Tel: +86-25-84303406, E-mail: jzliu@njust.edu.cn
DOI: 10.1016/S1003-6326(23)66384-8

with good bonding quality. Among them, roll-bonding is considered to be the most economical and promising process for industrial application due to its advantages in relatively low cost and high production rate [18]. Up to now, various metal laminated composites have been successfully achieved via roll-bonding with/without post-heat treatment, and the effect of rolling parameters (such as rolling reduction and rolling temperature) on bonding quality and integrated mechanical property has been widely studied. For example, three-layered Ti/Cu/Ti clad materials were prepared by cold rolling at room temperature and the results indicated that higher post-heat treatment temperature accelerated the formation of inter-metallic compound at the interface and promoted the ductility of the laminated composites [19]. The 7B52 Al-alloy laminated composites were fabricated by hot-roll bonding techniques and good metallurgical bonding and straight interfaces were achieved [20]. Multilayer 1100/7075 laminated composites with excellent interface state were synthesized by hot accumulative roll bonding technology, and the effect of lamellar structural parameters on the bending fracture behavior was explored [21]. In addition, pure Al laminates with various heterostructures were engineered via extrusion, rolling and annealing, and the hetero-deformation induced (HDI) strengthening and strain hardening should be responsible for the superior mechanical property [22].

However, studies on the effect of thickness ratios on microstructure and mechanical property during rolling process are limited and the effect of subsequent precipitation behavior of synthesized laminates on microstructure and mechanical property has not been focused on. Hence, in the present study, Al (1060)/Al-alloy (7N01)/Al (1060) three-layered laminates with different thickness ratios (1:1:1, 1:2:1, 1:4:1) were designed and fabricated via hot rolling at 475 °C. The inner layer (7N01 Al-alloy) provided strength and the outer ones (pure Al) maintained a good corrosion resistance. The bonding interfaces were analyzed and the effects of layer thickness ratios on microstructure features and mechanical properties of the synthesized laminates were studied contrastively. Moreover, the significant effects of extra solution annealing and peak ageing treatment before cold rolling on the microstructure evolution and mechanical property were explored.

2 Experimental

The experimental materials used in this work are commercial Al-alloy 7N01 and pure Al 1060, and the chemical compositions are given in Table 1. Cold rolling was used to thin the initial 7N01 alloy and Al 1060 sheets (6 mm in thickness) down to different thickness (2, 3 and 4 mm for 7N01 alloy, and 1, 1.5 and 2 mm for Al 1060). The diagrammatic illustration of the experimental procedures is shown in Fig. 1. After homogenization annealing at 475 °C for 2 h, the sheets were cut into cuboids with length of 80 mm and width of 60 mm. After surface treatment, these 1060/7N01/1060 cuboids were stacked and fastened, to obtain initial sandwich structure with different constituent layer thickness ratios of 1:4:1, 1:2:1, and 1:1:1, respectively. Thus, the total thickness of the primary sandwich-structured sheets was 6 mm. After being preheated at 475 °C for 5 min, these sheets were roll-bonded immediately via a single-pass hot rolling. The rolling speed was 0.34 m/s, and the total thickness reduction was about 55%. For simplicity, the corresponding hot-rolled sheets with initial layer thickness ratios of 1:1:1, 1:2:1 and 1:4:1 were referred to as Sheet A, Sheet B, and Sheet C, respectively. The sheet C was then divided into two equal pieces. One was directly cold rolled (DCR) at room temperature with a total thickness reduction of ~60%, which was referred to as Sheet D. The other piece was first solution-annealed at 475 °C for 2 h, then artificial ageing at 120 °C for 48 h was performed in the oil bath furnace, and finally, the obtained specimen was suffered similar cold deformation (ACR), and the cold-rolled sample was marked as Sheet E.

Table 1 Chemical compositions of 7N01 Al-alloy and 1060 pure Al (wt.%)

Alloy	Zn	Mg	Cu	Mn	Fe	Si	Cr	Ti	Zr	Al
7N01	4.86	1.22	0.131	0.345	0.08	0.038	0.171	0.047	0.133	Bal.
1060	0.018	0.004	0.002	0.003	0.257	0.078	0.002	0.021	−	Bal.

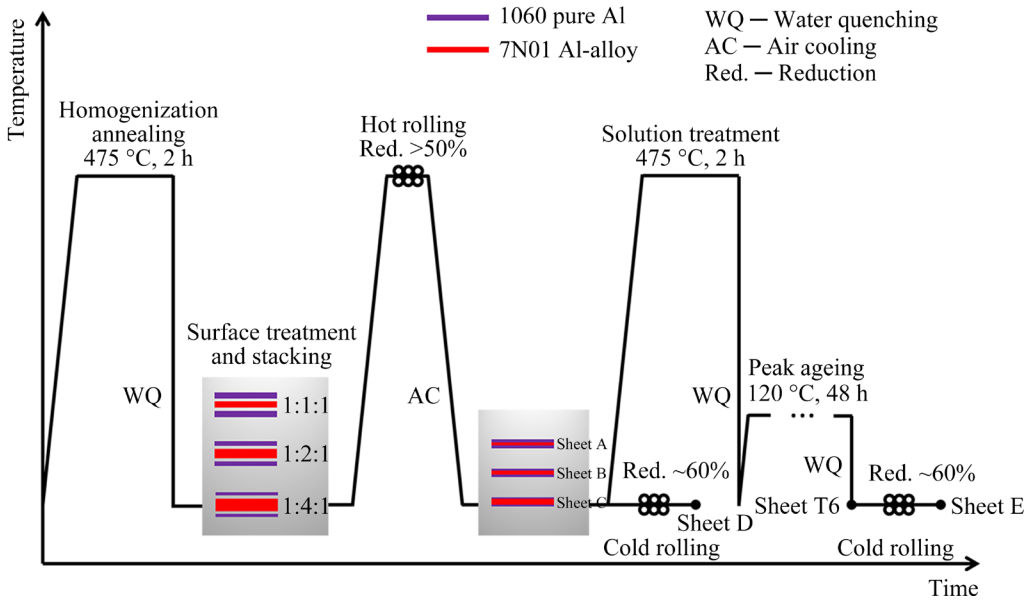

Fig. 1 Schematic illustration of experimental procedures

Microstructure and layer morphology of the composites were characterized via a scanning electron microscope (SEM, FEI Quanta 250F) equipped with an Oxford energy dispersive X-ray spectrometer (EDS), a Carl Zeiss Auriga crossbeam focused ion beam electron microscope equipped with electron backscattered diffraction (EBSD), and transmission electron microscope (TEM). All the samples were ground and polished using standard metallographic technique, and all the microstructure characteristics were captured from the rolling direction−transverse direction (RD−ND) sections. The EBSD examinations were performed at operating voltage of 15 kV, aperture of 120 mm, working distance of 14 mm, and step size of 0.4 μm. TEM examinations were conducted in FEI Titan G2 60−300 Cs-corrected HRTEM instrument operated at 300 kV.

Hardness measurements were performed using HMV−G 21DT micro Vickers hardness tester with an applied load of 0.49 N and a dwelling time of 10 s, and each hardness value is the average of more than 10 measurements. Flat dog-bone tensile specimens with gauge length of 5 mm and width of 2 mm were sectioned along RD. Uniaxial tensile tests were carried out at ambient temperature on an Instron−5982 testing machine with a crosshead speed of 0.3 mm/min. Three specimens were prepared for each condition to ensure the data reproducibility.

3 Results and discussion

3.1 Microstructural features of hot-rolled laminated composites

The microscopic morphologies of the hot-rolled laminated composites are shown in Fig. 2. No obvious cracks and voids can be seen at the straight bonding 1060/7N01 interfaces regardless of the constituent layer thickness ratios, as shown in Figs. 2(a−c), indicating that different layers are bonded together after single pass hot rolling with a thickness reduction higher than 50%. The thickness reduction of each layer in the three samples are calculated, as given in Table 2, according to the thickness change of the layers before and after hot rolling. Obviously, pure Al layers suffer larger deformation due to the superior plastic process-ability. In higher magnification (Fig. 2(d)), a few of discontinuous island-shaped oxides inlaid in the interface appear occasionally. TEM observations further prove that two types of interface morphologies have been formed during hot rolling. One is the straight and clean interface without any oxides (Fig. 2(e)), and the other is the formation of an oxidation transition layer between pure Al and 7N01 Al-alloys (Figs. 2(f, g)). Actually, the oxidation behavior at the interface is hard to avoid in this case due to the higher rolling temperature. The EDS map-scanning analysis of the transition

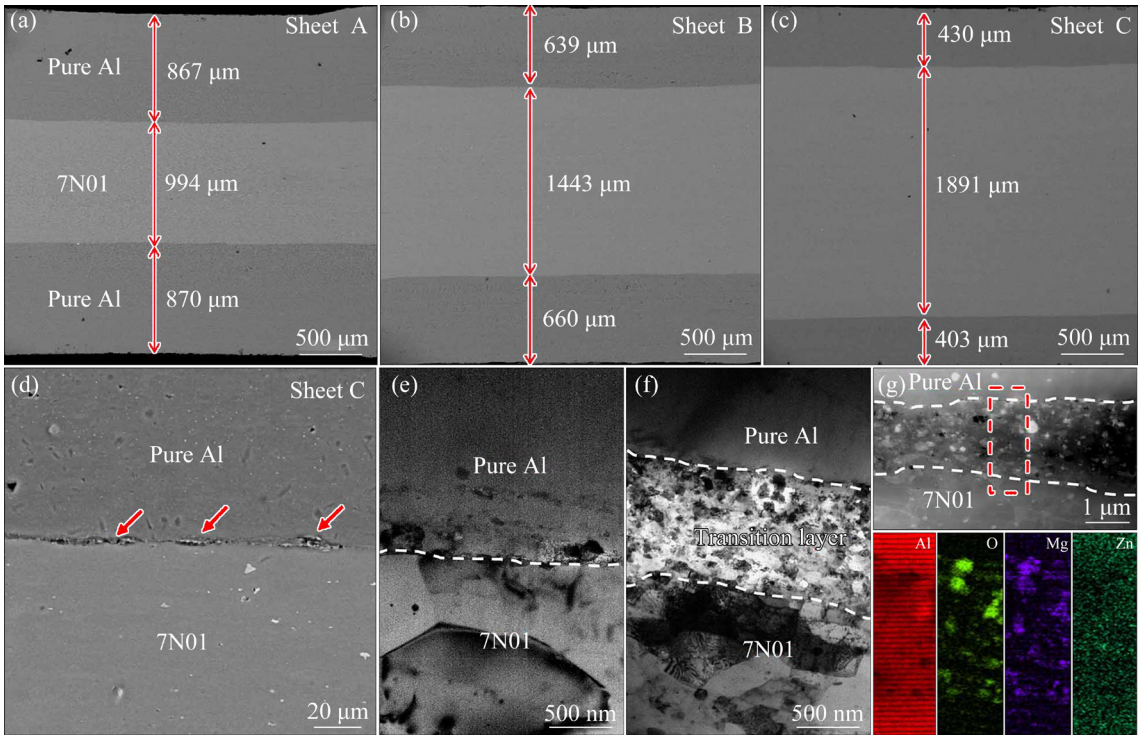

Fig. 2 Interface morphologies of hot-rolled laminated composites: (a−d) SEM image; (e, f) TEM images of Sheet C; (g) HAADF-STEM image and corresponding EDS map-scannings of interface morphologies of Sheet C

Table 2 Actual reduction of hot-rolled 1060/7N01/1060 laminated composites with various thickness ratios

Sheet	Reduction of 1060 layer/%	Reduction of 7N01 layer/%	Total reduction/%
A	56.6	50.3	54.5
B	56.7	51.9	54.3
C	58.3	52.7	54.6

layer shows that these compounds are mainly Mg−Al mixed oxides (Fig. 2(g)). Anyway, reliable interfacial metallurgical bonding between pure Al and Al alloy layers has been achieved except the occasionally appearance of small amounts of oxides.

The microstructure of pure Al and 7N01 layers after hot rolling were characterized by SEM and EBSD, respectively. Figures 3(a−c) show typical SEM micrographs of pure Al layers after hot rolling. As shown, dynamic recrystallization takes place, leading to the formation of equiaxed grains. The grain size of pure Al is measured carefully using the linear intercept method based on the SEM micrographs, and the corresponding grain size distribution histograms are shown in Figs. 3(d−f). The average grain size (AG) of pure Al layers of Sheets A, B and C are 1.53, 1.48 and 1.4 μm, respectively. As expected, higher thickness reduction results in finer grains.

EBSD analysis maps showing microstructure features of 7N01 layers are shown in Fig. 4. From the inverse pole figure (IPF) maps (Fig. 4(a)), one can note that the hot-rolled 7N01 layers in all the specimens are mainly composed of severe elongated grains. The grain size along normal direction is estimated based on the EBSD data, and the average values of Sheets A, B, C are 2.83, 2.95 and 2.87 μm, respectively (Fig. 4(d)). The corresponding grain boundary distribution histograms are also shown in Fig. 4(e), indicating that the percentage of high-angle grain boundary (HAGB) increases gradually with the increase in thickness of 7N01 Al-alloy layer. This indicates that the microstructure in 7N01 layers does not undergo obvious recrystallization. The corresponding recrystallization distribution maps (Fig. 4(b)) give direct experimental evidences for this. The percentages of different grain types of the three hot-rolled specimens are summarized in Fig. 4(f). This should be attributed to the higher recrystallization temperature (~370 °C) of 7N01 Al-alloys and the short duration during hot rolling. Corresponding

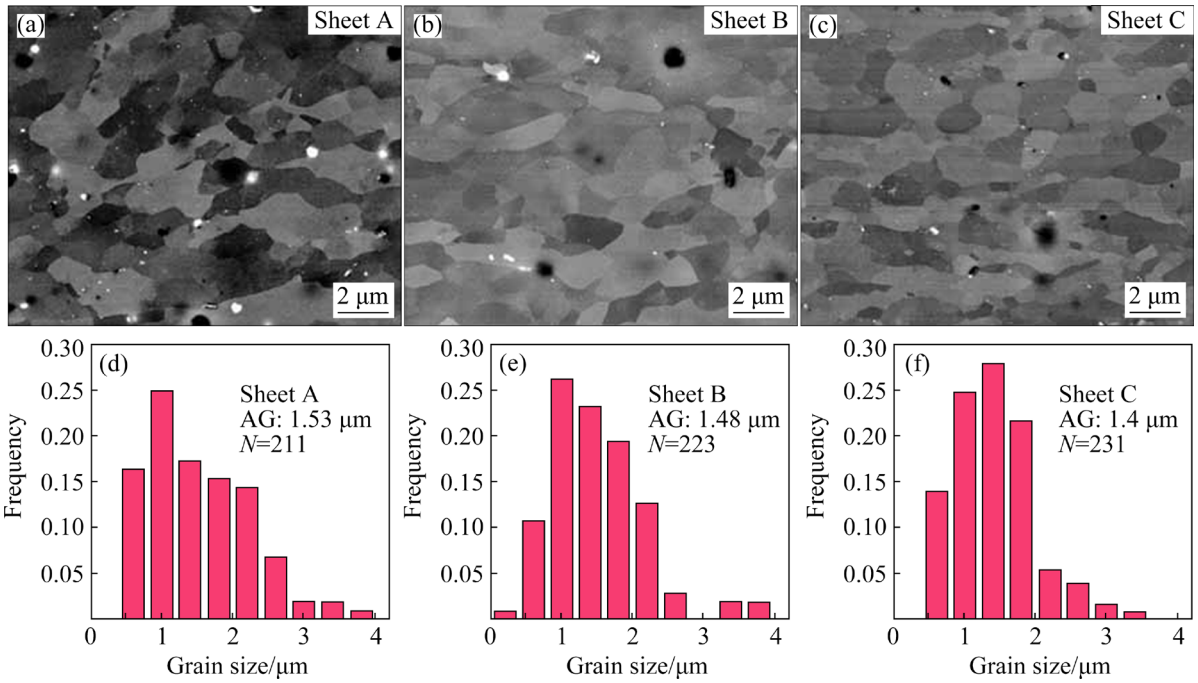

Fig. 3 SEM images (a−c) and corresponding grain size distribution histograms (d−f) of pure Al layers of Sheet A, Sheet B and Sheet C (AG−Average grain size; *N*−Number of measured grains)

Kernel average misorientation (KAM) maps are shown in Fig. 4(c). KAM maps give a direct vision on the distribution of micro-strain, and higher KAM value refers to higher number of dislocation density because local misorientation is proportional to geometrically necessary dislocations [23]. The measured average KAM values of the three hot-rolled samples are 1.14°, 1.05° and 1.03°, respectively. Sheet C has the lowest KAM value, indicating a relatively stronger dynamic recovery and recrystallization effects, which is in accord with the results in Fig. 4(b). The higher deformation degree in 7N01 layers of Sheet C may accelerate the recovery and recrystallization processes.

The hot-rolled microstructure in 7N01 layer of Sheet C was further characterized by TEM observation, as shown in Fig. 5. The elongated grains with ~3.6 μm in width are observed in Figs. 5(a, b), which is in accord with the EBSD results (Fig. 4). It can be found that the large elongated grains mainly consist of tangled dislocations and many sub-grains. The insert in Fig. 5(a) shows the selected area electron diffraction (SAED) pattern of the low angle grain boundary with the misorientation angle of ~8.3°. Additionally, large amounts of particles are formed dynamically during hot rolling, which can be clearly captured from the HAADF-STEM micrograph (Fig. 5(c)). The corresponding elements mapping images of the selected area (Fig. 5(d)) indicate that the larger rod-like particle is formed by the enrichment of Mn and Cr elements, and the small ones (marked by 1−3) contain the Mg and Zn elements. EDS composition analysis displayed in Table 3 shows that these small precipitations are $MgZn_2$ phases.

3.2 Mechanical properties of hot-rolled laminated composites

The hardness of pure Al and 7N01 layers in the hot-rolled laminated composites are presented in Fig. 6(a). The micro-hardness of pure Al layers keeps a same value of 0.37 GPa regardless of the constituent layer thickness ratios, showing similar degrees of dynamic recrystallization, which is consistent with SEM observation (Fig. 3). For the 7N01 layers, the average hardness value decreases slightly from 1.05 to 0.98 GPa, with the increase in the thickness of 7N01 layers. The gentle softening must be related to the decrease of the amounts of deformed structure (Fig. 4), which corresponds to the increase of thickness reduction (Table 2).

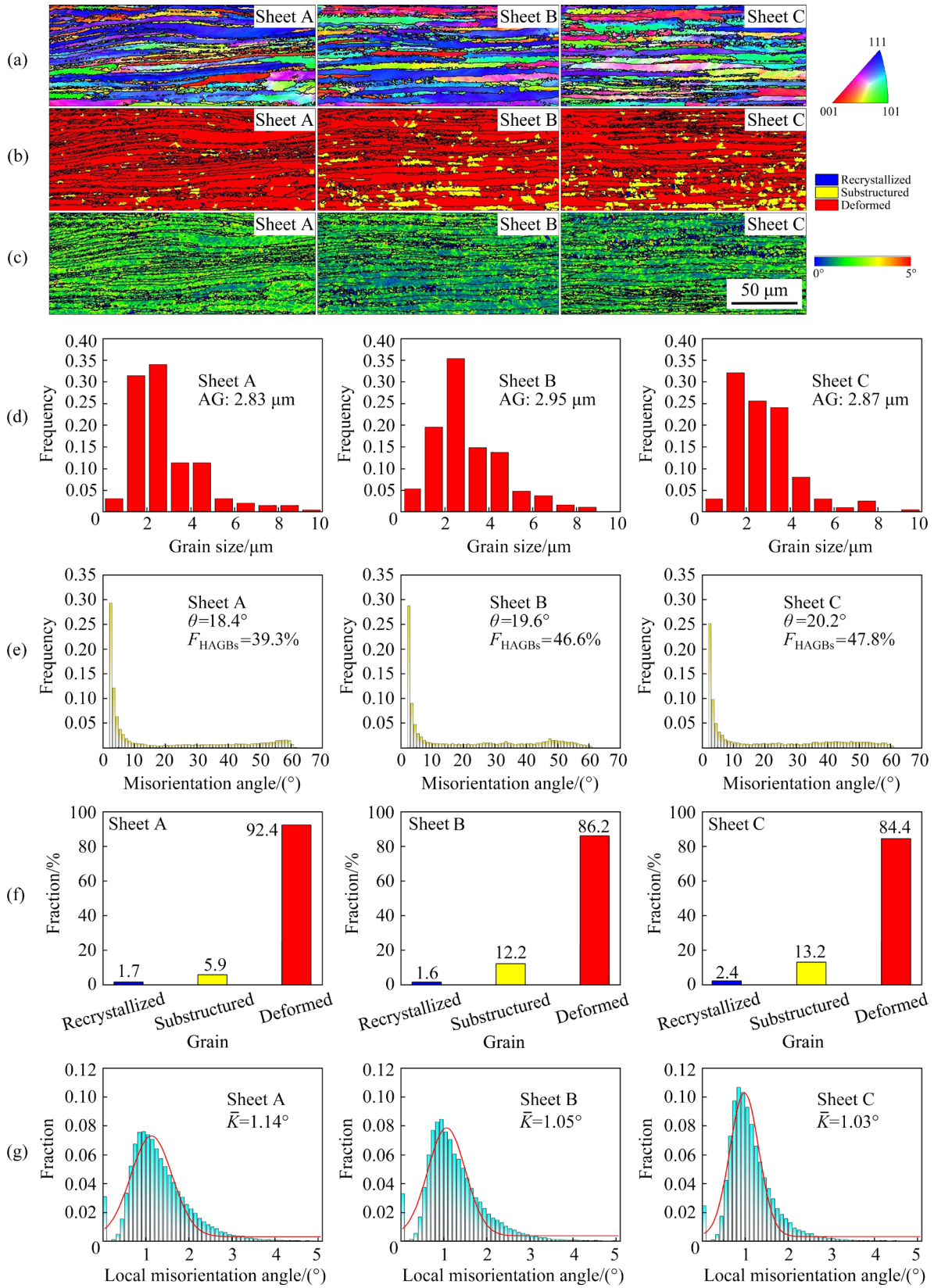

Fig. 4 EBSD analysis maps of 7N01 layers: (a) IPF maps; (b) Recrystallization distribution maps; (c) KAM maps; (d) Grain size distribution histograms; (e) Misorientation angle distribution histograms; (f) Relative proportion of different types of grains for samples; (g) KAM distribution histograms (The average grain size (AG), the average orientation angle (θ), the fraction of high-angle grain boundaries (F_{HAGBs}) and the average KAM values ($\bar{K}$) are also shown)

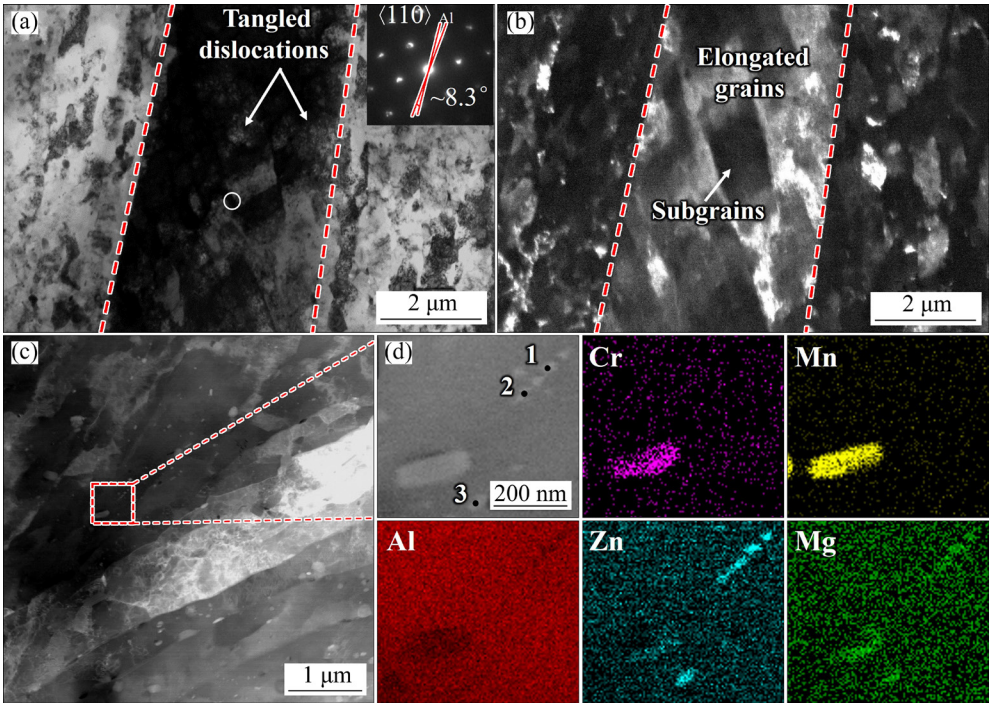

Fig. 5 Bright (a) and dark (b) field TEM micrographs of 7N01 layer for Sheet C; (c) HAADF-STEM image observed along $\langle 112\rangle_{Al}$ zone axis showing existence of particles; EDS mappings (d) of red dotted line frame in (c)

Table 3 Chemical compositions obtained by EDS point scanning in Fig. 5(d) (at.%)

Point No.	Al	Zn	Mg
1	96.5	2.35	1.15
2	97.36	1.72	0.93
3	97.36	1.84	0.8

Figure 6(b) shows the engineering stress−engineering strain plots of hot-rolled laminated composites, and the mechanical properties are summarized in Fig. 6(d). Undoubtedly, the hot-rolled 7N01 Al-alloy exhibits much higher strength and better uniform elongation than the hot-rolled 1060 pure Al. However, for the hot-rolled laminated composites, the values of yield strength (0.2% strain offset stress) of Sheets A−C are measured as 180, 210 and 240 MPa, respectively. Their values of tensile strength are 196, 239 and 279 MPa, respectively. Both the yield strength and tensile strength increase greatly with increasing the proportion of 7N01 Al-alloy component. Meanwhile, the ductility (uniform elongation) is also improved gently from 6.3% of Sheet A to 8.4% of Sheet C. The good strain hardening ability should be responsible to the considerable ductility.

For the laminated composite structure, the yield strength (σ_s) and uniform elongation (ε_{UE}, true strain) can be expressed as [24,25]

$$\sigma_s = \sum V_i \sigma_{i,s} \tag{1}$$

$$\varepsilon_{UE} = \frac{\sum V_i \sigma_{i,UE} \varepsilon_{i,UE}}{\sum V_i \sigma_{i,UE}} \tag{2}$$

where V_i and $\sigma_{i,s}$ are the volume fraction and yield flow stress of the component i (1060 pure Al and 7N01 Al alloy), respectively; $\sigma_{i,UE}$ and $\varepsilon_{i,UE}$ refer to the true stress and true strain of the component i at necking point, respectively. The theoretically predicted values of yield stress from the rule of mixture (ROM) are 176, 214 and 250 MPa, respectively, indicating a good agreement between experimental results and theoretical calculations. With regards to ductility, the calculated values of uniform elongation (true strain) from ROM of Sheets A, B and C are 0.048, 0.054 and 0.058, respectively. The predicted values are obviously lower than the experimental observations (they are 0.06, 0.065 and 0.08, respectively). It seems that extra strain hardening has been introduced in the laminated sheets, which leads to a tensile ductility higher than predication by the ROM. Similar phenomenon has been reported in a coarse-grained/nanostructure laminate material [26]. The authors

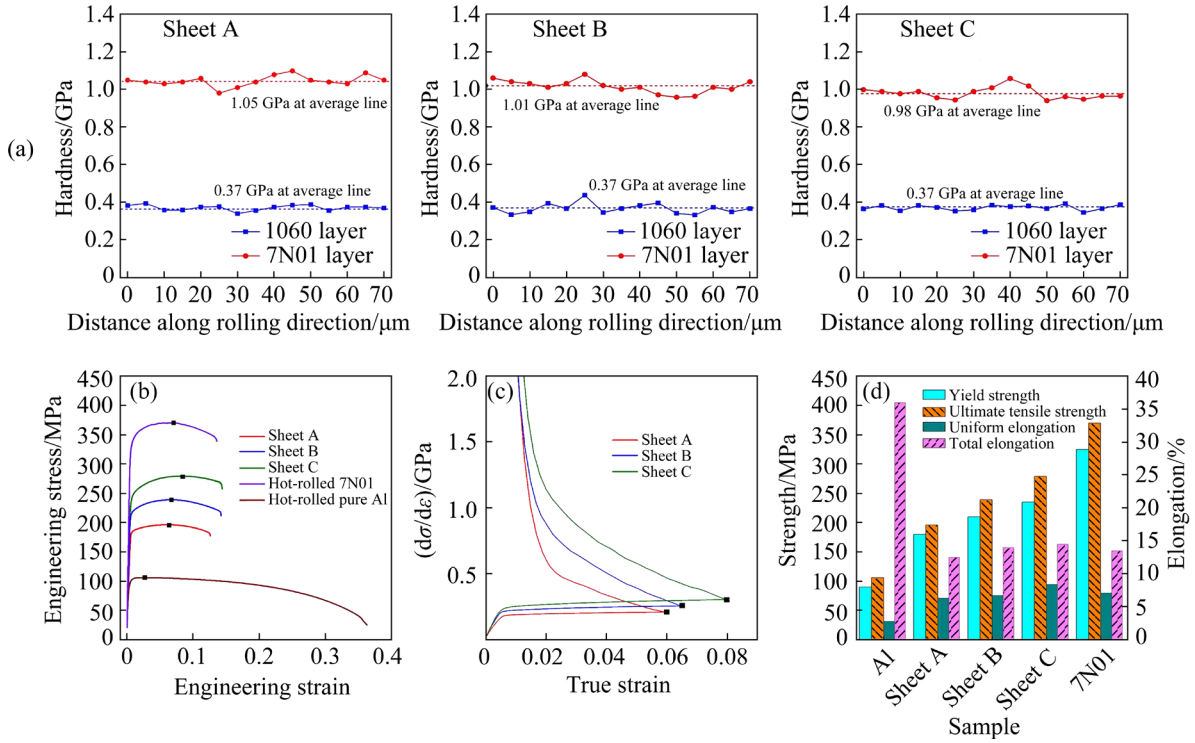

Fig. 6 Hardness in 7N01 Al-alloy and pure Al layers (a); engineering stress−engineering strain curves (b); strain hardening rate curves (c); comparison of tensile properties of experimental materials of hot-rolled laminated composites with various thickness ratios (d)

stated that the well-bonded interface maintained the overall uniform deformation for the whole sample, and mechanical incompatibility between different layers during tensile deformation generated high strain hardening. In this case, pure Al layers have limited uniform elongation owing to the lack of sufficient strain hardening capacity, while the 7N01 alloy has considerable strain hardening capacity (Fig. 6(b)). Thus, the outer pure Al layers start necking early at deformation stage. However, this necking process is stopped by the middle 7N01 layer. The formation of instable outer layers and stable middle layer mutually restrict each other, resulting in the converting from uniaxial applied tensile stress to bi-axial stresses [26]. As a result, geometrically necessary dislocations (GNDs) are generated and pile up around the interface in order to accommodate the mechanical incompatibility across the interface, which can produce an extra strain hardening [27].

As can be seen in Fig. 6(c), Sheet C with layer thickness ratio of 1:4:1 exhibits the highest strain hardening ability. It is conventionally believed that the strain delocalization and strain gradients originate from the internal stress induced by deformation incompatibility between constituent layers during the tensile deformation [28]. However, local stress state and strain distributions can be significantly affected by layer thickness ratio. XIA et al [29] have shown that layer thickness ratios can change the affected zone range of strain gradients in constituent layers. They found that when the volume fraction of soft layer was reduced to a certain extent, the compressive strain gradient regions could cover the entire soft layer, leading to significant improvement of strain hardening ability. Thus, it is basically reasonable that the overall performance of Sheet C is better than that of the other two laminates. In addition, the heterogeneous interfaces with strain gradients can produce a hetero-deformation induced (HDI) hardening effect, which can simultaneously improve strength and ductility [30,31].

3.3 Effect of DCR and ACR treatment on microstructure features

As can be seen in Fig. 5, $MgZn_2$-type precipitates are formed during hot rolling. Different features of dynamic precipitates and static ones may exist, and it should be meaningful to explore their

effects on the corresponding mechanical property. Thus, the hot-rolled Sheets C were selected to perform the subsequent DCR and ACR treatment, respectively, due to its good strength−ductility combination. During the ACR processing, the ageing time is very critical for precipitation evolution. As shown in Fig. 7, the micro-hardness of 1060 pure Al layer remains largely unchanged (~0.24 GPa) during ageing regardless of holding time. However, for the 7N01 alloy layer, the hardness values increase rapidly from 0.67 to 1.05 GPa at first stage (0−12 h), then followed by a relatively moderate increase before reaching a peak value (1.25 GPa at 48 h), and finally a slight decrease with further extension of ageing time. Similar phenomenon has been reported in previous studies [32−34]. When ageing at 120 °C for 0−48 h, the formation of GP zones (GPI and GPII) and metastable η' phase is believed to be responsible for the age hardening in this system [35,36]. However, the subsequent softening stems from the formation of the incoherent η phase particles [35].

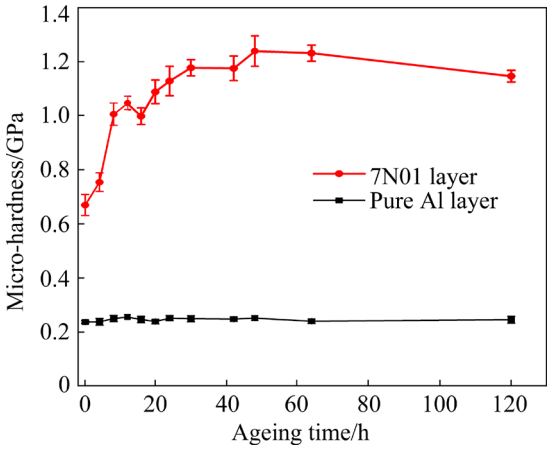

Fig. 7 Hardness evolution of 7N01 alloy and pure Al layers during ageing at 120 °C

Samples after ageing at 120 °C for 48 h, marked as Sheet T6 (Fig. 1), were prepared for EBSD and TEM observations, as shown in Fig. 8. For the pure Al layer, obvious grain growth occurs and the average grain size reaches ~30 μm. Compared to the hot-rolled samples (Fig. 6(a)), the hardness decrease of pure Al layer should be mainly due to grain coarsening during solution annealing and peak ageing, as shown in Fig. 8(a). The heat treatments also make a slight softening (from 0.98 to 0.67 GPa) in 7N01 alloy layers. As can be seen, though most of the grains still keep stretching, static recrystallization has occurred and many ultrafine grains (~0.41 μm) with straight and clear boundaries are formed in these elongated grains (Fig. 8(b)). In addition, abundant nano-scaled precipitates have been formed during the peak ageing, which can be observed clearly in the HAADF-STEM image (Fig. 8(c)). It is reasonable to consider that these particles belong to GP zones and η' phase, which has been verified by many previous studies [34−36]. Larger spherical one indicated by red arrow is believed to be Al_3Zr [37].

The effects of DCR and ACR treatment on the microstructure features of 1060 pure Al layers are shown in Fig. 9. The equiaxed grains are stretched along the rolling direction. The grain size has been refined to varying degrees versus their corresponding initial microstructure. Careful analysis reveals that the average values of grain size of pure Al layers in Sheets D and E are 0.64 and 0.7 μm, respectively.

Above SEM observation shows that the extra solution annealing and peak ageing treatments almost have no effects on the grain size of pure Al layers. However, two obvious differences can be captured in the microstructure of 7N01 alloy layers.

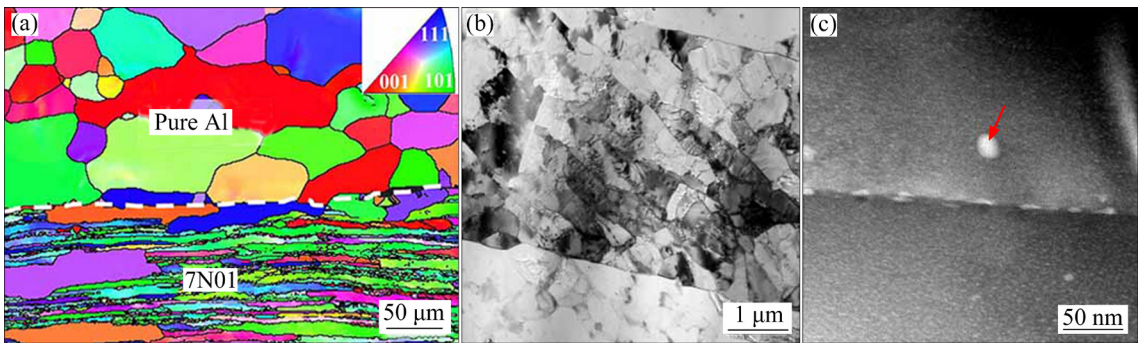

Fig. 8 Microstructural characteristics of Sheet T6: (a) IPF map; (b) Bright-field TEM image of 7N01 layer; (c) HAADF-STEM image of 7N01 layer obtained along $\langle 112 \rangle_{Al}$ zone axis

As shown in Fig. 10, strip-like grains with large numbers of tangled dislocations are formed during cold rolling in both samples. However, the average width of these grains in Sheet E is ~185 nm, which is much smaller than that in Sheet D (~330 nm). Another important difference is the formation of precipitates, as shown in Figs. 10(c, f). Obviously, the particles in Sheet E are much finer than those in Sheet D, and the density is also much higher. It can be concluded that the precipitates in Sheet D mainly inherit from the hot-rolled microstructures (Fig. 5(c)), which are stable η phases. However,

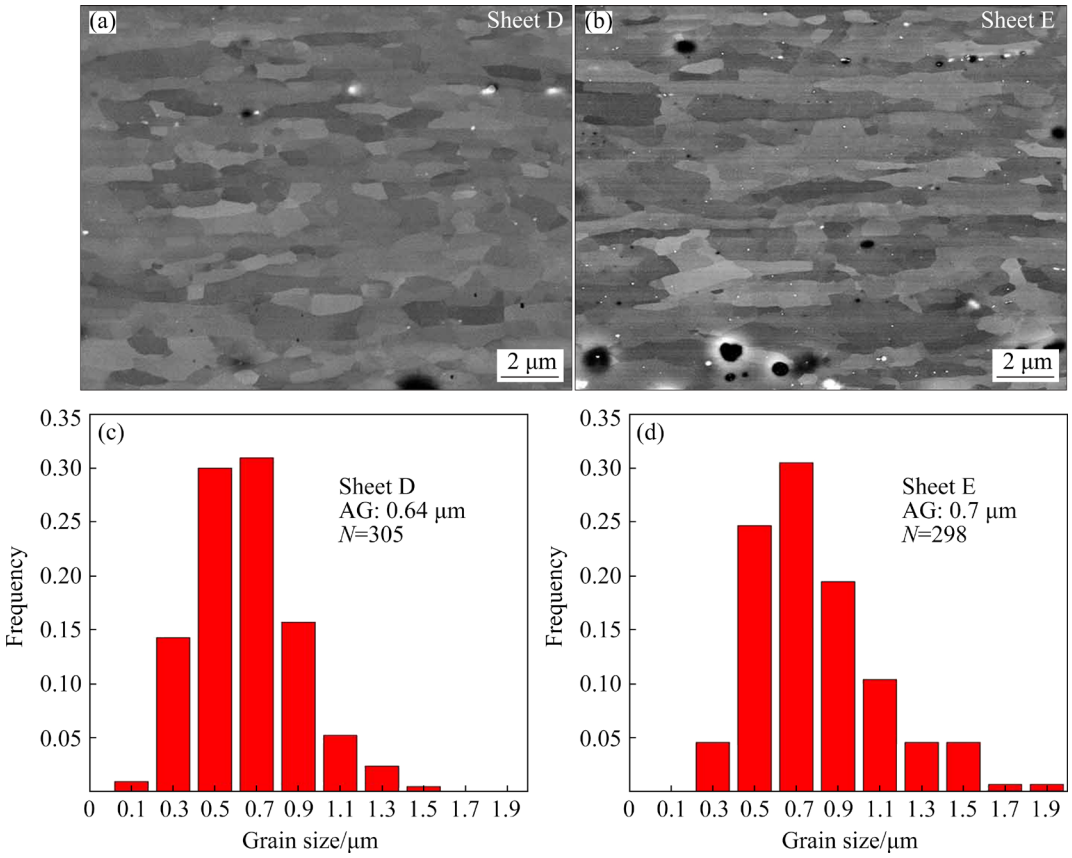

Fig. 9 SEM micrographs (a, b) and corresponding grain size distributions (c, d) of pure Al layer of cold-rolled samples

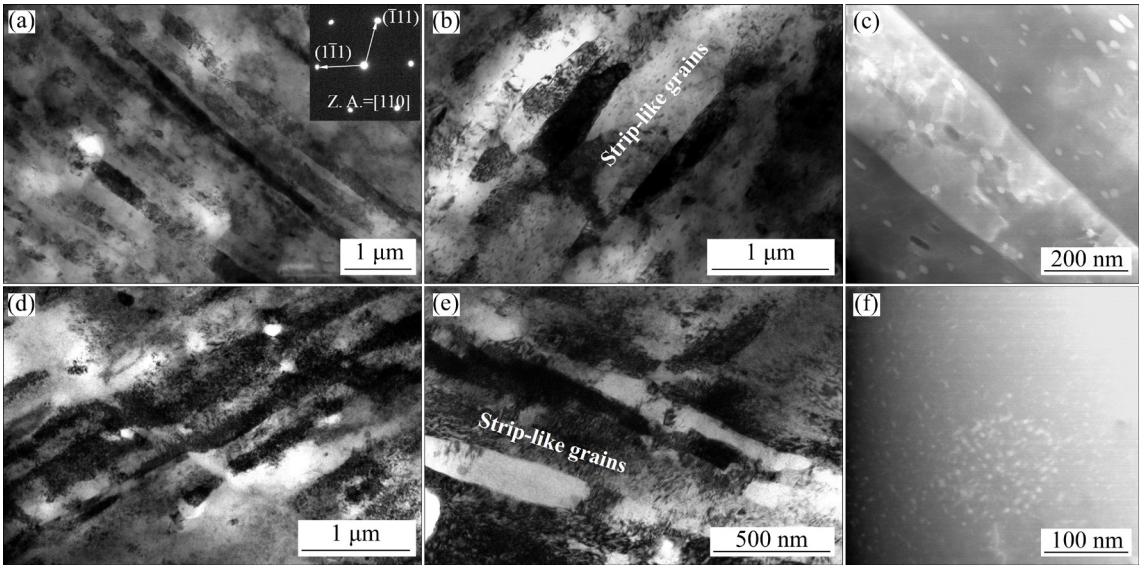

Fig. 10 Typical TEM micrographs of Sheet D (a, b) and Sheet E (d, e), and HAADF-STEM images of Sheet D (c) and Sheet E (f) obtained along $\langle 112 \rangle_{Al}$ zone axis

redissolution of these particles takes place during solution annealing at 475 °C for 2 h. Therefore, the finer precipitations in Sheet E must stem from the subsequent peak ageing treatment. Different from the coarser particles in Sheet D, these precipitates in Sheet E should be mainly metastable η' phases having semi-coherent interfaces with Al matrix, which is considered as the main strengthening phase in T6 condition [38]. And this conclusion keeps well accordance with the hardness variation trend (Fig. 7). In addition, the stronger pinning effect of the finer precipitates in Sheet E results in the formation of dense dislocation tangles, leading to higher dislocation density, as can be seen in Figs. 10(d, e).

3.4 Effect of DCR and ACR treatment on mechanical properties

Comparisons of engineering stress−strain curves of cold-rolled samples are shown in Fig. 11(a), and the corresponding mechanical properties are summarized in Table 4. For comparison, the mechanical property of T6 sample is also given, and its values of yield strength and tensile strength are 258 and 287 MPa, respectively. After cold rolling, Sheet E has high strength (yield strength of 360 MPa and tensile strength of 369 MPa) but poor ductility (uniform elongation of ~1.3%). Although the yield strength and tensile strength of Sheet D are ~15% and 14% lower than those of Sheet E, the uniform elongation and total elongation are increased by ~130% and 160% to 3% and 6.5%, respectively. Strain hardening rate ($d\sigma/d\varepsilon$) curves are shown in Fig. 11(b). It can be found that there are two typical strain hardening stages including a steep decrease stage at small strain and a steady-state one at larger strain. However, Sheet E has no obvious steady-state work hardening stage, and the strain hardening rate decreases rapidly at a small strain (<0.013) till necking. By comparison, Sheet D has superior work hardening ability due to the higher strain hardening rate at the whole strain stage.

It can be seen from Fig. 8 that obvious grain growth has occurred in both pure Al layer and 7N01 layer. Meanwhile, abundant static precipitates are formed in 7N01 layer after solution treatment and peak ageing. Similar mechanical properties between Sheet C and Sheet T6 indicate that the strengthening effect caused by static precipitates

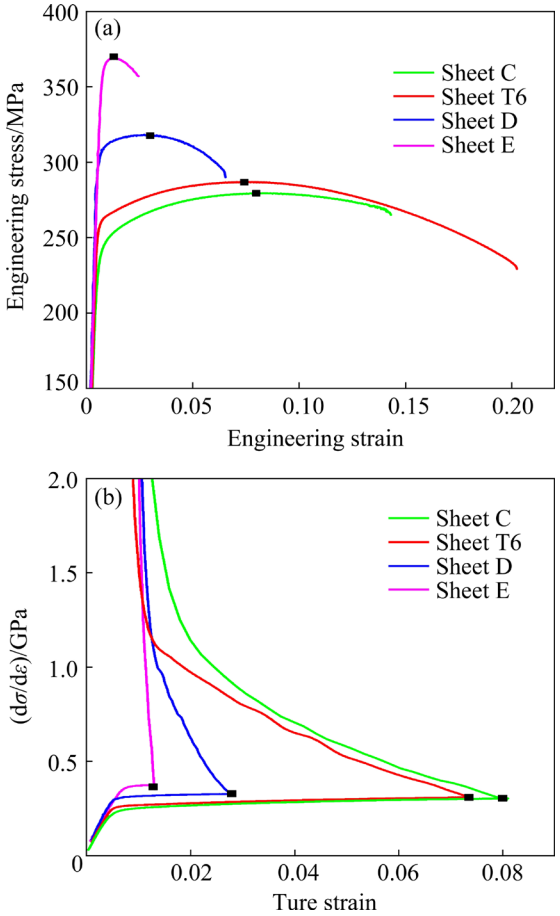

Fig. 11 Mechanical properties after heat treatment and cold rolling treatment: (a) Engineering stress−strain curves; (b) Strain hardening rate curves

Table 4 Tensile properties after heat treatment and cold rolling treatment

Sheet	Yield strength/MPa	Ultimate tensile strength/MPa	Uniform elongation/%	Total elongation/%
C	240	279	8	14.3
T6	258	287	7.4	20
D	305	318	3	6.5
E	360	369	1.3	2.5

can compensate for the strength loss due to dislocation recovery, grain coarsening and redissolution of dynamic precipitates during solution treatment. The enhanced total elongation can be ascribed to better deformation coordination ability of the coarse and free-dislocation grains. For cold-rolled samples, the microstructure discrepancy between Sheets D and E is not significant for the pure Al layers, as shown in Fig. 9. Thus, the effect of soft pure Al layers on the whole strength should

be limited. As to the 7N01 Al-alloy layer, three important microstructure differences exist between Sheets D and E. First, the width of strip-like grains formed during cold rolling in Sheet D is larger than that in Sheet E (Figs. 10(b, e)). According to the classical Hall−Petch relation [39], stronger grain refinement strengthening can be generated in Sheet E. Second, finer precipitates with higher density can be seen in Sheet E (Figs. 10(c, f)), which is formed during peak ageing. These particles in Sheet E should mainly be semi-coherent η' phase, while the larger ones in Sheet D is believed to be stable η phase, which is non-coherent with Al matrix. Therefore, stronger precipitation strengthening should be formed in Sheet E. Third, the finer, more dense and semi-coherent η' phase can be more effective in hindering dislocation movement, resulting in higher dislocation density after cold rolling (Figs. 10(d, e)), leading to a stronger dislocation strengthening. Thus, the synergy effect of multi-strengthening mechanisms makes Sheet E much stronger. However, initial higher dislocation density in cold-rolled Sheet E makes follow-up dislocations difficult to slip and accumulate during subsequent tensile testing. This causes pre-mature necking of Sheet E without evident strain hardening (Fig. 10), which is typical tensile feature of severely deformed metals [40,41].

4 Conclusions

(1) The 1060/7N01/1060 laminated composites with reliable interfacial metallurgical bonding have been achieved via single-pass hot rolling at 475 °C. Microstructure features of hot-rolled sheets are similar, regardless of layer thickness ratios. Equiaxed grains with average grain size of ~1.5 μm are formed in pure Al layers, and large elongated grains (~3.6 μm in width) containing tangled dislocations and many sub-grains are observed in 7N01 alloy layer.

(2) The experimental data of yield strength keep good agreement with theoretical analysis based on the rule of mixture. However, extra strain hardening induced by well-bonded interfaces results in better practical tensile ductility. A good strength−ductility combination along with considerable strain hardening ability is obtained in the hot-rolled 1060/7N01/1060 sheets with layer thickness ratio of 1:4:1.

(3) Extra solution annealing and peak ageing treatment has nearly no influence on the microstructural features of pure Al layers. However, two obvious differences can be captured in the 7N01 layers. Compared to the DCR sheets, the strip-like grains in 7N01 layers of ACR samples are further refined from 330 to 185 nm, and the precipitates with higher density inherited from the ageing processing are also much finer. Thus, grain refinement strengthening and stronger precipitation strengthening and dislocation strengthening make the ACR specimens much stronger than the DCR ones.

CRediT authorship contribution statement

Shun-qiang LI: Methodology, Investigation, Writing − Original draft; **Guo-sheng SUN:** Conceptualization, Investigation, Writing − Original draft, Writing − Review & editing; **Rui-sheng ZHANG:** Investigation; **Xiao CHENG:** Investigation; **Ji-zi LIU:** Conceptualization, Resources, Writing − Review & editing, Funding acquisition.

Declaration of interests

The authors declare that they have no known competing financial interests or personal relationships that could have appeared to influence the work reported in this paper.

Acknowledgments

This work was supported by the National Natural Science Foundation of China (No. 52171119) and the Natural Science Foundation of Jiangsu Province, China (No. BK20201308). The authors are thankful for the technical support from the Jiangsu Key Laboratory of Advanced Micro & Nano Materials and Technology, China.

References

[1] ZHU Qian-qian, CAO Ling-fei, WU Xiao-dong, ZOU Yan, COUPER M J. Effect of Ag on age-hardening response of Al−Zn−Mg−Cu alloys [J]. Materials Science and Engineering A, 2019, 754: 265−268.

[2] LERVIK A, THRONSEN E, FRIIS J, MARIOARA C D, WENNER S, BENDO A, MATSUDA K, HOLMESTAD R, ANDERSEN S J. Atomic structure of solute clusters in Al−Zn−Mg alloys [J]. Acta Materialia, 2021, 205: 116574.

[3] YANG X B, CHEN J H, ZHANG G H, HUANG L P, FAN T W, DING Y, YU X W. A transmission electron microscopy study of microscopic causes for localized-corrosion morphology variations in the AA7055 Al alloy [J].

Journal of Materials Science & Technology, 2018, 34: 1719−1729.

[4] WANG Yi-chang, WU Xiao-dong, YUE Lu, GUO Ming-xing, CAO Ling-fei. Aging precipitation behavior and properties of Al−Zn−Mg−Cu−Zr−Er alloy at different quenching rates [J]. Transactions of Nonferrous Metals Society of China, 2022, 32(4): 1070−1082.

[5] YU Ming-yang, ZHANG Yong-an, LI Xi-xu, WEN kai, XIONG Bai-qing, LI Zhi-hui, YAN Li-zhen, YAN Hong-wei, LIU Hong-wei, LI Ya-an. Effect of recrystallization on plasticity, fracture toughness and stress corrosion cracking of a high-alloying Al−Zn−Mg−Cu alloy [J]. Materials Letters, 2020, 275: 128074.

[6] LI Xiu-yan, LU K. Improving sustainability with simpler alloys [J]. Science, 2019, 364(6442): 733−734.

[7] CHEN Zhi-qing, WANG Dong-ya, CAO Xiao-qing, YANG Wen-wu, WANG Wen-xian. Influence of multi-pass rolling and subsequent annealing on the interface microstructure and mechanical properties of the explosive welding Mg/Al composite plates [J]. Materials Science and Engineering A, 2018, 723: 97−108.

[8] SARAVANAN S, RAGHUKANDAN K. Microstructure, strength and welding window of aluminum alloy−stainless steel explosive cladding with different interlayers [J]. Transactions of Nonferrous Metals Society of China, 2022, 32(1): 91−103.

[9] PAUL H, PETRZAK P, CHULIST R, MAJ Ł, MANIA L, PRAŻMOWSKI, M. Effect of impact loading and heat treatment on microstructure and properties of multi-layered AZ31/AA1050 plates fabricated by single-shot explosive welding [J]. Materials & Design, 2022, 214: 110411.

[10] CHEN Xiang, HUANG Guang-sheng, LIU Shuai-shuai, HAN Ting-zhuang, JIANG Bin, TANG Ai-tao, ZHU Yun-tian, PAN Fu-sheng. Grain refinement and mechanical properties of pure aluminum processed by accumulative extrusion bonding [J]. Transactions of Nonferrous Metals Society of China, 2019, 29(3): 437−447.

[11] CHEN Xiang, ZHANG Jun-lei, XIA Da-biao, HUANG Guang-sheng, LIU Ke, JIANG Bin, TANG Ai-tao, PAN Fu-sheng. Microstructure and mechanical properties of 1060/7050 laminated composite produced via cross accumulative extrusion bonding and subsequent aging [J]. Journal of Alloys and Compounds, 2020, 826: 154094.

[12] FENG Guang-jie, WEI Yan, HU Bing-xu, WANG Yi-feng, DENG De-an, YANG Xiu-xia. Vacuum diffusion bonding of Ti_2AlNb alloy and TC4 alloy [J]. Transactions of Nonferrous Metals Society of China, 2021, 31(9): 2677−2686.

[13] LIN Peng, XI Xian-zheng, ZHAO Wen-kai, YANG Rui-hong, LIN Fei, CUI Xiao-lei, LIU Gang. Microstructure and mechanical properties of Ti−6Al−4V/Ti−22Al−25Nb joint formed by diffusion bonding [J]. Transactions of Nonferrous Metals Society of China, 2021, 31(5): 1339−1349.

[14] BAKHTIARI ARGESI F, SHAMSIPUR A, MIRSALEHI S E. Preparation of bimetallic nano-composite by dissimilar friction stir welding of copper to aluminum alloy [J]. Transactions of Nonferrous Metals Society of China, 2021, 31(5): 1363−1380.

[15] MENG Jian-bing, DONG Xiao-juan, ZHAO Yu-gang, XU Ru-feng, BAI Xue, ZHOU Hai-an. Fabrication of a low adhesive superhydrophobic surface on Ti6Al4V alloys using TiO_2/Ni composite electrodeposition [J]. Micromachines, 2019, 10(2): 121.

[16] BOBZIN K, BRÖGELMANN T, KALSCHEUER C, YILDIRIM B, LIANG T. Deposition of a nanocomposite (Ti,Al,Si)N coating with high thickness by high-speed physical vapor deposition [J]. Materialwissenschaft und Werkstofftechnik, 2020, 51(3): 297−312.

[17] WANG Wei, WEI Xiao-jun, WANG Chuan-shen, ZHOU Wen-cai, ZHU Bai-lin, WANG Chong-jie, LIU Lin-fei. Fabrication and thermo stability of the SnO_2/Ag/SnO_2 tri-layer transparent conductor deposited by magnetic sputtering [J]. Ceramics International, 2021, 47(3): 3548−3552.

[18] GHALEHBANDI S M, MALAKI M, GUPTA M. Accumulative roll bonding—A review [J]. Applied Sciences, 2019, 9(17): 3627.

[19] KIM Y K, POURALIAKBAR H, HONG S I. Effect of interfacial intermetallic compounds evolution on the mechanical response and fracture of layered Ti/Cu/Ti clad materials [J]. Materials Science and Engineering A, 2020, 772: 138802.

[20] ZHOU Gu-xin, LANG Yu-jing, HAO Jie, LIU Wen, WANG Sheng, QIAO Li, CHEN Min. Interface analysis of 7B52 Al alloy laminated composite fabricated by hot-roll bonding [J]. Transactions of Nonferrous Metals Society of China, 2016, 26(5): 1269−1275.

[21] MO Tai-qian, CHEN Ze-jun, ZHOU Da-yu, LU Guang-ming, HUANG Yong-meng, LIU Qing. Effect of lamellar structural parameters on the bending fracture behavior of AA1100/AA7075 laminated metal composites [J]. Journal of Materials Science & Technology, 2022, 99: 28−38.

[22] CHEN Xiang, ZHANG Bao-xuan, ZOU Qi, HUANG Guang-shen, LIU Shuai-shuai, ZHANG Jun-lei, TANG Ai-tao, JIANG Bin, PAN Fu-sheng. Design of pure aluminum laminates with heterostructures for extraordinary strength-ductility synergy [J]. Journal of Materials Science & Technology, 2022, 100: 193−205.

[23] LU Qun-jie, ZHENG Jin-yang, HUANG Gai, LI Ke-ming, DING Hui-ming, WANG Zheng-yu, CHENG Shao-an. Enhancing combined cryogenic mechanical properties of metastable austenitic stainless steel by warm forming [J]. Journal of Materials Processing Technology, 2021, 291: 117017.

[24] WU X L, JIANG P, CHEN L, ZHANG J F, YUAN F P, ZHU Y T. Synergetic strengthening by gradient structure [J]. Materials Research Letters, 2014, 2(4): 185−191.

[25] SEMIATIN S L, PIEHLER H R. Deformation of sandwich sheet materials in uniaxial tension [J]. Metallurgical Transactions A, 1979, 10(1): 85−96.

[26] MA X L, HUANG C X, XU W Z, ZHOU H, WU X L, ZHU Y T. Strain hardening and ductility in a coarse-grain/nanostructure laminate material [J]. Scripta Materialia, 2015, 103: 57−60.

[27] ZHOU Hao, HUANG Chong-xiang, SHA Xue-cha, XIAO Li-rong, MA Xiao-long, HÖPPEL H W, GÖKEN M, WU Xiao-lei, AMEYAMA K, HAN Xiao-dong, ZHU Yun-tian. In-situ observation of dislocation dynamics near heterostructured interfaces [J]. Materials Research Letters, 2019, 7(9): 376−382.

[28] JIANG S, PENG R L, HEGEDS Z, GNAUPEL-HEROLD T, MOVERARE J J, LIENERT U, FANG F, ZHAO X, ZUO L,

JIA N. Micromechanical behavior of multilayered Ti/Nb composites processed by accumulative roll bonding: An in-situ synchrotron X-ray diffraction investigation[J]. Acta Materialia, 2021, 205: 116546.

[29] XIA Yi-ping, WU Hao, MIAO Ke-song, LI Xue-wen, XU Chao, GENG Lin, XIE Hong-lan, FAN Guo-hua. Effects of the layer thickness ratio on the enhanced ductility of laminated aluminum [J]. Journal of Materials Science & Technology, 2022, 111: 256−267.

[30] ZHU Yun-tian, AMEYAMA K, ANDERSON P M, BEYERLEIN I J, GAO Hun-jian, KIM H S, LAVERNIA E, MATHAUDHU S, MUGHRABI H, RITCHIE, R O, TSUJI N, ZHANG Xiang-yi, WU Xiao-lei. Heterostructured materials: Superior properties from hetero-zone interaction [J]. Materials Research Letters, 2021, 9(1): 1−31.

[31] KIM J G, BAEK S M, LEE H H, CHIN K G, LEE S, KIM H S. Suppressed deformation instability in the twinning-induced plasticity steel-cored three-layer steel sheet [J]. Acta Materialia, 2018, 147: 304−312.

[32] MAHATHANINWONG N, PLOOKPHOL T, WANNASIN J, WISUTMETHANGOON S. T6 heat treatment of rheocasting 7075 Al alloy [J]. Materials Science and Engineering A, 2012, 532: 91−99.

[33] LIU J Z, CHEN J H, LIU Z R, WU C L. Fine precipitation scenarios of AlZnMg(Cu) alloys revealed by advanced atomic-resolution electron microscopy study. Part II: Fine precipitation scenarios in AlZnMg(Cu) alloys [J]. Materials Characterization, 2015, 99: 142−149.

[34] LIU J Z, CHEN J H, YANG X B, REN S, WU C L, XUB H Y, ZOU J. Revisiting the precipitation sequence in Al−Zn−Mg-based alloys by high-resolution transmission electron microscopy [J]. Scripta Materialia, 2010, 63(11): 1061−1064.

[35] ZHAO Yong-hao, LIU Ji-zi, TOPPING T D, LAVERNIA E J. Precipitation and aging phenomena in an ultrafine grained Al−Zn alloy by severe plastic deformation [J]. Journal of Alloys and Compounds, 2021, 851: 156931.

[36] ZANG Jin-xin, ZHANG Kun DAI Sheng-long. Precipitation behavior and properties of a new high strength Al−Zn−Mg−Cu alloy [J]. Transactions of Nonferrous Metals Society of China, 2012, 22(11): 2638−2644.

[37] SENKOV O N, SHAGIEV M R, SENKOVA S V, MIRACLE D B. Precipitation of $Al_3(Sc,Zr)$ particles in an Al−Zn−Mg−Cu−Sc−Zr alloy during conventional solution heat treatment and its effect on tensile properties [J]. Acta Materialia, 2008, 56: 3723−3738.

[38] YANG Wen-chao, JI Shou-xun, ZHANG Qian, WANG Ming-pu. Investigation of mechanical and corrosion properties of an Al−Zn−Mg−Cu alloy under various ageing conditions and interface analysis of η' precipitate [J]. Materials & Design, 2015, 85: 752−761.

[39] HANSEN N. Hall−Petch relation and boundary strengthening [J]. Scripta Materialia, 2004, 51: 801−806.

[40] XU Run-run, LIANG Ning-ning, ZHUANG Li-min, WEI Da-jie, ZHAO Yong-hao. Microstructure and mechanical behaviors of Al/Cu laminated composites fabricated by accumulative roll bonding and intermediate annealing [J]. Materials Science and Engineering A, 2022, 832: 142510.

[41] SU Li-hong, LU Cheng, LI Hui-jun, DENG Guan-yu. TIEU K. Investigation of ultrafine grained AA1050 fabricated by accumulative roll bonding [J]. Materials Science and Engineering A, 2014, 614: 148−155.

热处理对 1060/7N01/1060 轧制复合板显微组织及力学性能的影响

李顺强[1]，孙国胜[1]，张瑞升[1]，程 笑[1]，刘吉梓[1,2]

1. 南京理工大学 材料科学与工程学院 纳米异构材料中心，南京 210094；
2. 南京理工大学 分析测试中心，南京 210094

摘 要：利用 475 ℃单道次热轧的方式制备界面结合良好的 1060/7N01/1060 层状复合板。通过扫描电子显微镜、透射电子显微镜及电子背散射衍射结合硬度和拉伸实验研究层厚比对热轧复合板显微组织和力学性能的影响。此外，对比研究冷轧前热处理(固溶处理及峰值时效)对冷轧复合板显微组织和力学性能的影响。结果表明，层厚比对热轧复合板各层显微组织特征影响不大，其力学性能与混合法则理论预测结果一致。相比而言，额外的热处理对冷轧板纯铝层的晶粒尺寸无明显影响，却有助于细化 7N01 层的晶粒尺寸及弥散、细小析出物的形成，使其具有更显著的细晶强化、析出强化及位错强化效应。

关键词：7N01 铝合金；纯铝；层状复合板；结合界面；时效；力学性能

(Edited by Bing YANG)